Regular Article

# Dedicated STEM for 200 to 40 keV operation[⋆]

N. Dellby, N.J. Bacon, P. Hrncirik, M.F. Murfitt, G.S. Skone, Z.S. Szilagyi, and O.L. Krivanek[a]

Nion Co., 1102 8th St., Kirkland, WA 98033, USA
www.nion.com

**Abstract.** A dedicated STEM developed for operation at primary energies from 200 keV to 40 keV and lower is described. It has a new cold field emission gun (CFEG) that gives a normalized brightness of $3 \times 10^8$ A/(m$^2$ sr V), and excellent short-term and long-term stability. It includes two gun lenses (one electrostatic and one electromagnetic), a fast electrostatic beam blanker, three condenser lenses, a corrector of third- and fifth-order geometric aberrations, an objective lens with low aberration coefficients, a flexible set of projector lenses, an ultra-stable sample stage, and provision for storing up to five samples under high vacuum and loading them into the microscope's objective lens under remote control. The microscope is enclosed in a magnetically and acoustically shielding enclosure, which allows it to operate at a high performance level even in non-optimal environments. It has reached 53 pm resolution at 200 keV and 123 pm at 40 keV, and an EELS energy resolution of 0.26 eV.

## 1 Introduction

The ability of electron-optical instruments to form small electron probes has improved rapidly in the last decade. In 1999, two of the present authors co-wrote a paper entitled "Towards sub-Å electron probes" [1]. The stated goal seemed far-fetched at the time, but, with the help of a spherical aberration corrector, it was reached less than 3 years later in a dedicated scanning transmission electron microscope (STEM) operating at 120 keV [2]. Soon afterwards, several of the present authors started designing a whole new 200 keV STEM that incorporated a combined third- and fifth-order aberration corrector and an ultra-stable sample stage. They provided an early description of the design in a paper entitled "Towards sub-0.5 Å electron beams" [3]. We are now approaching this goal at 200 keV, as shown here, and it has already been reached by others at 300 keV [4,5] in TEM/STEMs. The richness of the new information unveiled by the improved capabilities can be seen in recent volumes dedicated to aberration-corrected electron microscopy (e.g., [6,7]).

The practical usefulness of a STEM is determined by many aspects of its performance and not just its probe size. Chief among these are the available probe current, the collection and detection efficiencies for various image and spectroscopy signals that the STEM is able to record, the electron energy loss spectroscopy (EELS) energy resolution, the STEM's ability to operate over a range of primary energies, and the vacuum level at the sample. EELS mapping becomes especially powerful when the probe current and the EELS collection efficiencies are increased substantially [8–12], and new insights into the electronic structure of materials become possible when the EELS energy resolution is improved [13,14]. Low primary energy operation avoids knock-on damage of low-$Z$ atoms, and a high vacuum free of water moisture and oxygen avoids chemically-assisted beam etching. Together they lead to largely damage-free imaging of materials such as graphene, single-sheet boron nitride, and carbon nanotubes [15–17].

Here we report on a new electron microscope designed to expand the present range of capabilities in all the above directions. The microscope is a dedicated STEM equipped with a cold field emission electron gun. It can operate at energies from 200 keV down to 40 keV and lower, reach a probe size <60 pm at 200 keV and ~123 pm at 40 keV, deliver 1 nA of current into a 200 keV probe <144 pm in size, and an energy resolution ~0.3 eV. The instrument would not exist without Christian Colliex, whose work on STEM and EELS provided an inspiration for it, and whose support was a crucial factor in the decision to develop the instrument. It is therefore very appropriate to dedicate this paper to him.

## 2 System construction

A scanning transmission electron microscope can be divided into five principal parts:

1. electron source that generates an electron beam, which should be as bright and monochromatic as possible;

---

2. probe-forming optics that focuses the electron beam onto the sample. It should be corrected for all the principal aberrations and able to produce an electron probe that is as small and stable as possible;
3. sample stage that is able to move the sample by small or large distances along five orthogonal axes ($X$, $Y$, $Z$, $\alpha$, $\beta$) and hold it still with sub-Å stability when the motion has stopped;
4. detection optics that couples the various signals into the appropriate detectors efficiently; and
5. detectors, which must detect the chosen signals with good sensitivity, large dynamic range, suitable speed and, in the case of spectroscopic signals, as good an energy resolution as possible.

There are many additional requirements, such as a high and clean vacuum near the sample, needed to avoid sample contamination and etching, flexible optics allowing the STEM to operate in many different modes at several primary energies, and powerful and user-friendly software that allows users to obtain high-quality results in a simple and convenient manner. As with many complex systems, a STEM becomes especially useful when all its parts have been thoroughly optimized.

The electron source is a crucial part of a STEM, just as important as the probe-forming optics. As discussed in detail in [18], the source brightness determines how rapidly the size of the electron probe formed by a STEM broadens at probe currents greater than zero. When the source contribution to the size of the electron probe becomes equal to the diffraction limit contribution, i.e., when the probe becomes $\sqrt{2}$ times greater than the size it would have in the limit of zero probe current, the probe current can be called the "coherent probe current" [18]. The coherent current defined in this way is a characteristic property of the source. In principle it is independent of the accelerating energy of the microscope, though in practice each particular CFEG produces the highest coherent current at the accelerating energy it has been optimized for. Typical coherent currents are 100–500 pA for a CFEG and 20–100 pA for a Schottky source. The higher coherent current plus the narrower energy distribution of the emitted electrons (about 0.3 eV full-width at half-maximum (FWHM) for the standard CFEG, about 0.6 eV for the standard Schottky sources) makes the CFEG the optimum source for probe-forming electron optics. We have therefore developed a CFEG for our 200 keV STEM.

With its small native source size, a CFEG can be sensitive to mechanical vibrations and requires thorough magnetic shielding. In addition, it needs a high-performance, ultra-high vacuum pumping system, and heat shields so that it can be baked at a temperature high enough for attaining an ultra-high vacuum in the $10^{-12}$ Torr range. These requirements are best served by placing the gun at the bottom of the electron column, a solution pioneered by VG instruments [19].

Figure 1 shows a schematic diagram of the Nion CFEG. Its electronics has been implemented as a "3-tank design," in which the high tension (HT) generation and sensing are done in two separate tanks, called the "multiplier"
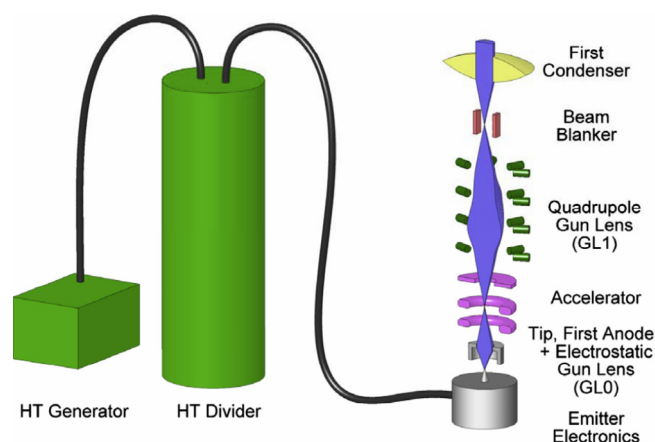


**Fig. 1.** (Color online) Schematic view of the principal components of the new CFEG.

and the "divider," respectively. This allows the HT sensing circuitry in the divider to be isolated from the 15 kHz frequency used by the Cockroft-Walton generator in the multiplier, so that spurious pick-up of this frequency does not affect the quality of the HT stabilization. The HT generator is insulated with oil for greater compactness and better heat dissipation. The HT divider and the gun chamber emitter electronics are insulated with $SF_6$ for reduced leakage currents and improved serviceability. An $SF_6$ recycling system is provided with the microscope, in order to avoid atmospheric discharges of the gas when servicing the gun or the divider.

The high tension is supplied to the emitter electronics on three separate conductors via a 3-core high voltage cable: HT, HT+25 V, and HT−16 V. The +25 V and −16 V supplies can provide up to 50 W of power for running the emitter electronics. The emitter electronics generates all the voltages and currents needed by the tip assembly: the extraction voltage, the focusing anode voltage, and the currents needed for tip flashing and for activating a miniature vacuum pump in the vicinity of the tip. Much thought has gone into the protection of the field-emitting tip and of the emitter electronics against discharges. The result is that the tip is typically able to survive even discharges occurring during conditioning at 240 kV. The field emission tip is W $\langle 3\ 1\ 0 \rangle$, typical of standard cold field emission sources.

The gun vacuum system consists of three 30 l s$^{-1}$ ion pumps, one of which provides differential pumping isolation from the rest of the column, and three separate titanium sublimation pumps. After changing the emitter, the gun is baked at 240 °C, and the emitter assembly is thoroughly cleaned by electron bombardment. This provides a vacuum near the tip that is well below the X-ray limit (about $2.3 \times 10^{-11}$ Torr) of the hot-cathode ion gauge used to measure the gun pressure. When emitting, the pressure increases by about $1 \times 10^{-11}$ Torr. The pumping isolation from the rest of the column is about 1:25000, which means that vacuum in the $10^{-8}$ Torr range in the first condenser lens just above the gun does not affect the gun operation.

The emitter assembly includes a focusing electrode (electrostatic gun lens, called GL0), which is able to vary the divergence of the beam emerging from the emitter assembly independently of the extracted current. The acceleration from the emitter assembly to the full 200 keV beam energy is accomplished in three stages differing by 66 kV (and proportionately less at lower beam voltages). It is designed to be as rapid as possible, while avoiding fields high enough to cause discharges. This is done in order to minimize the time the electrons travel at a low energy, when they are especially susceptible to brightness-decreasing stochastic Coulomb interactions.

The final (ground potential) anode is followed by a short flight tube and two electromagnetic deflectors, which align the beam on a differential pumping aperture of 200 $\mu$m diameter. The next optical element is a 4-quadrupole electromagnetic lens assembly (quadrupole gun lens, called GL1). The quadrupoles are run weakly, with no beam crossovers inside the quadrupole assembly. The quadrupole gun lens also includes sextupole lenses, which allow second-order geometrical aberrations (primarily 3-fold astigmatism) originating inside the gun and the gun lenses to be corrected. The whole assembly is equivalent to a weak round lens with minimized $C_s$ and $C_c$ aberration coefficients and an ability to control first- and second-order aberrations. The double deflector and the quadrupole gun lens have been designed to withstand the full gun bake temperature, and there are no cold spots in the gun during a bake. Above the quadrupole gun lens, there is an electrostatic beam blanker, which is able to blank the beam in about 2 $\mu$s. The beam blanker module also provides thermal insulation between the gun, which is baked at 240 °C, and the rest of the column, which is baked at 140 °C.

In normal operation, the electrostatic GL0 and the electromagnetic GL1 are used together to produce a crossover at the beam blanker and either one crossover (as shown in the figure) or no crossovers before the beam blanker. A crossover at the center of the blanker minimizes the beam excursion at the sample when the blanker is activated, and also minimizes beam jitter when the beam blanker is off and electrical noise manages to couple into it. Varying the ratio of the focal length of the two gun lenses allows the convergence of the beam at the beam blanker to be varied, and using the two gun lenses in conjunction with the first condenser allows the demagnification of the electron source seen by the rest of the electron-optical column to be adjusted as necessary. This arrangement also provides the flexibility to keep the gun optical properties essentially constant as the emitter tip ages and blunts, and to operate the CFEG near its optimum over a range of accelerating energies.

A cross-section of the gun as well as of the rest of the column is shown in Figure 2. The column from the first condenser lens on is similar to the 100 keV STEM column we have described previously [8], with two principal differences: the objective lens has been redesigned to allow 200 keV operation, and there is more X-ray shielding. The column includes three round condenser lenses, and
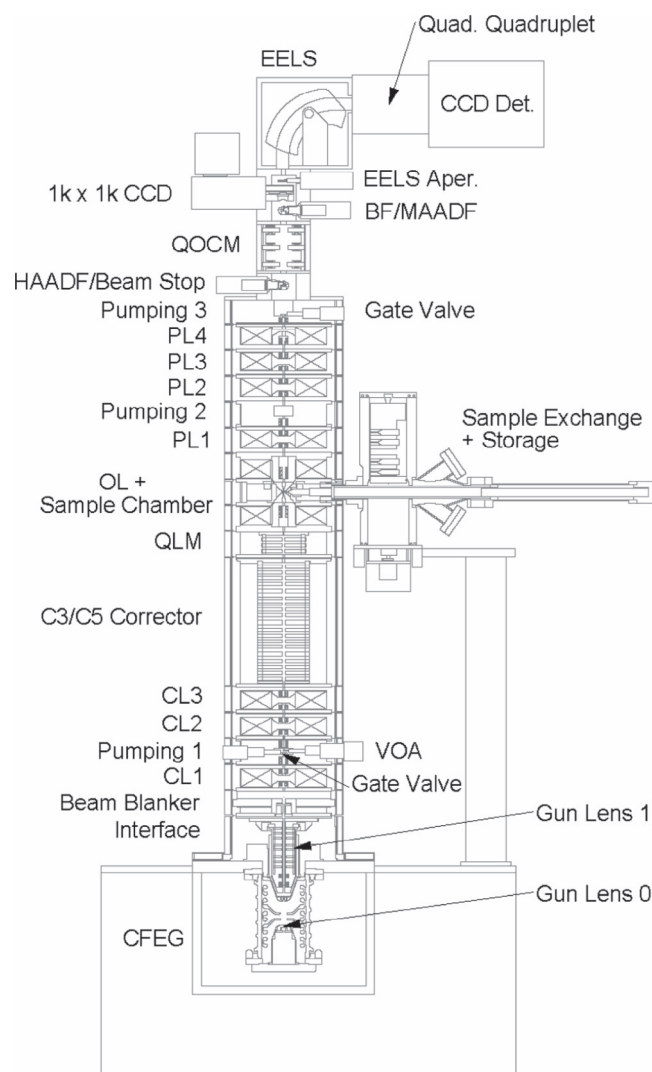


**Fig. 2.** Cross-section of the microscope column of the UltraSTEM$^{TM}$200.

a corrector of third- and fifth-order geometric aberrations [20, 21], and a quadrupole lens module (QLM) that images the corrector into the objective lens, a condenser-objective lens with a gap of 4 mm, a focal length of 2 mm, and aberration coefficients $C_s$ and $C_c$ both close to 1 mm, four round projector lenses and a quadrupole-octupole coupling module (QOCM). An alternate objective lens pole-piece with an 8-mm gap and $C_s$ and $C_c$ close to 2 mm is also available.

The QOCM is able to adjust the first-, second-, and third-order aberrations affecting the electron energy loss spectrometer (EELS), and is also able to change the camera length of the diffraction pattern detected on the system's Ronchigram-recording CCD camera and the bright field (BF)/medium angle annular dark field (MAADF) detectors, which are all placed after the QOCM. The QOCM does not change the camera length at the high-angle annular dark field (HAADF) detector, which is placed just in front of it. The camera length at the Ronchigram CCD

33505-p3

and the BF and MAADF detectors can therefore be set independently of the camera length at the HAADF detector. Switching the QOCM from one setting to another does not result in noticeable hysteresis, and it does not change the field distributions appreciably in the round lens part of the column. This means that switching, using the QOCM, from the camera length needed for Ronchigram observation to the camera length needed by the HAADF, MAADF, BF and EELS detectors does not change the focus of the probe, whereas changing the setting of a round projector lens can easily produce a small change in the magnetic field in front of the sample, leading to a small but noticeable change in probe focus.

In normal operation, the microscope is run with the sample-level beam crossover a few $\mu$m above the center of the objective lens, i.e., with the second half of the objective lens too weak to form a focused image of the sample. Deliberate underfocusing of the post-sample part of the objective lens counteracts the effect of the lens's spherical aberration, and it improves the collection efficiency for high-angle electrons on the HAADF and MAADF detectors. A disadvantage of this regime is that the sample height has to be changed and the microscope retuned in order to operate with a focused conventional (fixed-beam) image, as a STEM/CTEM. In other words, in order to improve the collection efficiency for the MAADF and HAADF detectors, we normally operate the microscope as a dedicated STEM rather than a STEM/CTEM, even though the combined mode is also possible in the Nion UltraSTEM$^{TM}$. To be truly useful, however, the CTEM mode of the microscope would probably need a post-sample aberration corrector and a larger format CCD camera than $1k \times 1k$, which are developments we may well undertake in the future.

An electron energy loss spectrometer (EELS), typically a Gatan Enfina or Quantum, is placed at the end of the detector column. The QOCM is able to produce a virtual crossover at the precise height required by the EELS optics. Using a virtual rather than a real EELS entrance crossover means that the physical separation of the EELS from the last projector lens (P4) can be shortened, resulting in a saving of about 20 cm in the total height of the column relative to a system in which the EELS uses a real entrance crossover. Another important role of the QOCM is to null geometric aberrations affecting the EELS up to third order, i.e., to work as a compact pre-EELS aberration corrector. The correction includes overcoming the spherical aberration contributed by the post-sample field of the objective lens. The strength of this contribution at the QOCM grows as $(1/(\text{pre-EELS camera length}))^4$. The QOCM is able to null it for camera lengths down to about 20 mm (measured at the EELS entrance aperture), allowing the EELS to accept scattering half-angles up to about 75 mrad (through a 3-mm diameter entrance aperture), without a noticeable worsening of the EELS energy resolution. In regular practice, collection angles into the EELS only slightly larger than the bright field cone semi-angle of 25–35 mrad are typically used, and scattering half-angles of the order of 75 mrad are collected by the MAADF detector. But a safety margin that allows even larger angles to be collected into the EELS without running into problems with EELS aberrations is useful for various situations such as optimizing the collection efficiency for EELS mapping using high-energy loss edges.

Up to five sample cartridges can be pre-loaded into a sample magazine, which is stored in an ion-pumped sample storage chamber next to the microscope column. Each cartridge can be transferred into the microscope column under computer-automated local or remote control. Cartridges developed so far include fixed tilt cartridges for regular 3-mm diameter samples and for rectangular samples up to $7 \times 7$ mm, a fixed tilt cartridge that lowers the sample by 1 mm and is useful for double-crossover imaging described further on in the paper, a tilting cartridge providing $\pm 25$ degrees of tilt in two orthogonal directions, and an electrical contacts cartridge that brings up to six separate voltages to a 3-mm diameter microfabricated sample. The cartridges are decoupled from the external world when inside the microscope, and the sample stage motion is precise enough to move the sample by as little as 1 nm in $X$ and $Y$, and 5 nm in $Z$ [22]. In stable environments, the stage drift is typically better than 1 Å/min, which means that compositional maps requiring total acquisition times of several minutes can be formed without any drift compensation.

Vacuum sealing of the microscope column is done by copper gaskets and metal C-rings. The vacuum at the sample is typically in the $10^{-9}$ Torr range, and it can be improved into the $10^{-10}$ or even $10^{-11}$ Torr range by baking and careful sample handling. Despite the very high level of the attainable vacuum, the entire column is modular, with a small copper gasket seal between all adjacent column modules. As a result, it is possible to change various key elements of the column even in the field. For instance, Nion's first 200 keV STEM (delivered to Christian Colliex's laboratory) has been provided with both the standard (4-mm gap) objective lens (OL) sample chamber, and a second sample chamber with a larger OL gap (8 mm) optimized for in situ experiments, and the two chambers will be switched as needed. The modular column should also allow major future additions, such as a post-sample CTEM corrector, or a monochromator presently being developed at Nion [23].

## 3 Performance

The performance of the new microscope is documented in Figures 3–9. Figure 3 shows a high-angle annular dark field (HAADF) image of a multiply-twinned gold nanoparticle lying on a thin carbon film obtained at 200 keV with 15 pA of beam current at 32 $\mu$s per each $12 \times 12$ pm large pixel, with a probe convergence semi-angle of 32 mrad. The multiple twinning gave rise to different crystallographic orientations in different parts of the particle, and to various lattice fringe spacings. The Fourier transform (FT) inset shows that spatial frequencies corresponding to 56 pm have been captured in this image. The FT comes from a larger image area which included five other particles.
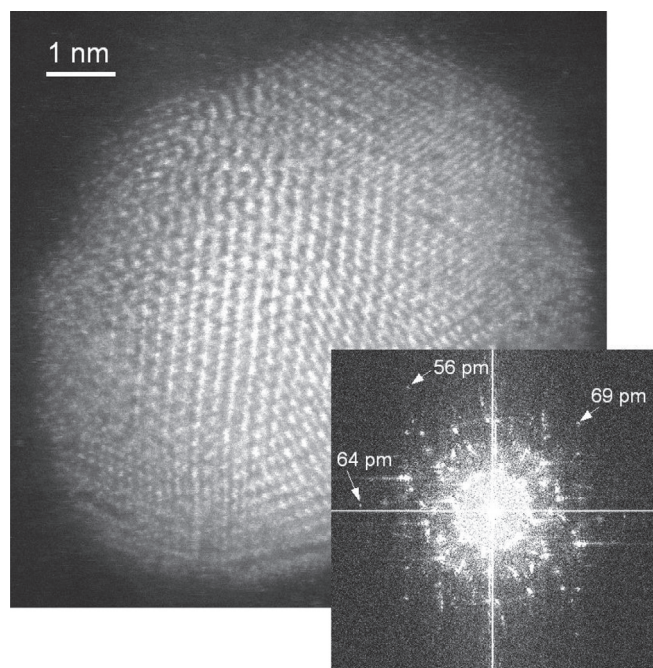
**Fig. 3.** Unprocessed HAADF image of a multiply-twinned gold particle recorded at 200 keV with 15 pA beam current. The inset shows a Fourier transform (diffractogram) of the image demonstrating captured spacings as small as 56 pm.



**Fig. 4.** Fourier transforms of an HAADF image of a gold particle demonstrating strong transfer of spatial frequencies due to lattice spacing of 53 pm. 200 keV, 30 pA beam current. The scan directions were rotated 90° for the second image.

beam current chosen for Figure 3 minimized the particle movement, and it allowed us to explore the attainable resolution determined by the microscope's optics rather than by the virtual source size.

Being able to reach HAADF resolutions of the order of 50 pm is confirmed experimentally in Figure 4, which shows a pair of Fourier transforms of two HAADF images of a gold particle acquired at 200 keV with 30 pA probe current. The highest spatial frequency transferred is $(53 \text{ pm})^{-1}$, with good strength. To confirm that the $(53 \text{ pm})^{-1}$ spots were not an artifact caused by a lower spatial frequency spot combining with an instability of a well-defined frequency, we acquired the particle image twice, with the scan directions rotated by 90° for the second image. The same pattern of reflections appears in both FTs, confirming that the spots correspond to spacings present in the sample.

Figure 5 shows an HAADF image of another gold nanoparticle obtained at 200 keV with a CFEG extraction current of 10 μA. The probe half-angle was 20 mrad and the probe current 1.07 nA. Using a probe current of this order and a smaller illumination convergence angle than the largest value allowed by the aberration performance of the microscope allows the gun brightness to be determined more accurately. The image shows strong 144 pm fringes due to (2 2 0) gold planes. The high-current image is less "crisp" (more "wobbly") than the 15 pA image shown in Figure 3, and this is a consequence of gold particles moving and changing under a high-current probe. A stationary 200 keV probe of 1 nA will in fact drill a hole in a small gold particle in a few seconds. Two other reasons for the increased image "wobbliness" are that a large beam current is obtained by demagnifying the source less, which means that any jitter of the source is also demagnified less, and further that the wider beam extracted from the gun, as needed for the larger current, is more sensitive to stray fields and other instabilities.

As described in reference [18], when the probe current is not zero, the probe size $d_p$ is broadened relative to the diffraction-limited probe size $d_o$ as

The marked 69 pm spacing (and weaker 64 and 67 pm spacings, not marked in the FT) come from the shown particle, the other two marked spacings come from other particles in the same image.

The Fourier transform shows an absence of vertical streaks, which typically result when the probe "jitters" relative to the sample (or the sample jitters relative to the probe) by more than about 1/5th of the image resolution. This indicates that the short-term stability of the probe in the new microscope is at least as good as the roughly 0.1 Å r.m.s. stability attained by Nion's 100 keV STEM [24]. It is telling that the image was recorded while the microscope was still at Nion, in a very non-optimized environment, during working hours. It shows that the microscope is much less sensitive to external disturbances than what has lately become the norm in electron microscopy.

Gold nanoparticles have several advantages as test samples, such as the availability of many different spacings, an easily recognizable large-area parallel-beam diffraction pattern that is highly suitable for characterizing camera lengths, and compatibility with standard autotuning algorithms. They have become the standard sample for testing the microscope performance at Nion. But they also have some disadvantages. The lattice planes that are resolved depend on the particles' orientations, which are random, and finding a particle with suitable test spacings is therefore not systematic. The gold particles tend to move under the beam, especially at primary energies higher than about 60 keV, which cause damage in the supporting carbon film. This means that image "jitters" can appear even when the microscope itself is actually quite stable. The low
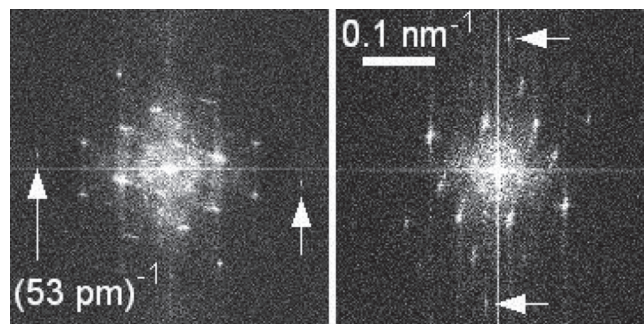
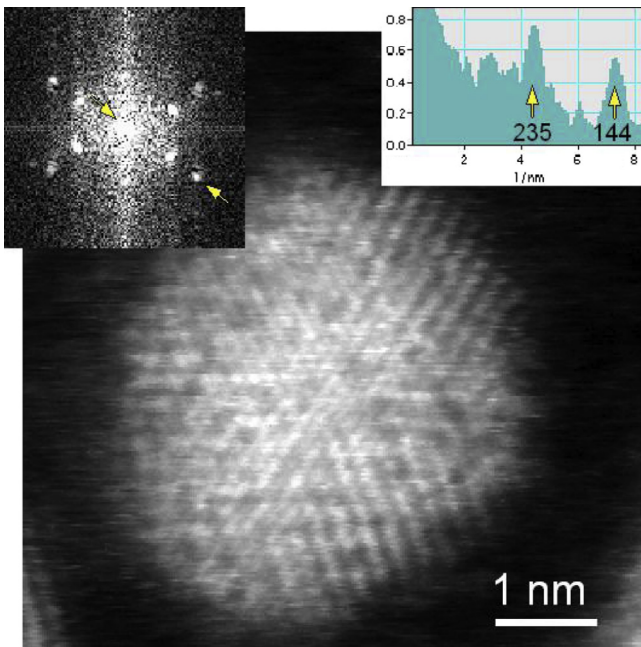$$d_p = (1 + I_p/I_c)^{0.5} d_o, \qquad (1)$$

**Fig. 5.** (Color online) Unprocessed HAADF image of a gold particle recorded at 200 keV with 1.07 nA current contained in a probe with 20 mrad semi-angle. The Fourier transform inset shows strongly transferred spacings of 144 pm. The profile inset displays an intensity profile through the FT (taken between the yellow arrows), and shows that the transfer strength of the 144 pm spacings was only about 30% weaker than the transfer of 235 pm spacings from another part of the same particle.

where the diffraction-limited probe size is given by $d_o = 0.61\lambda/\alpha_o$, $\lambda$ is the electron wavelength, $\alpha_o$ the probe half-angle, $I_p$ the probe current, and $I_c$ the coherent current of the source.

For a 20 mrad probe half-angle, $d_o$ at 200 keV is 77 pm. Assuming that the probe diameter was similar to the 144 pm strongly transferred to the image, we can then determine $I_c$ as

$$I_c = I_p d_o^2/(d_p^2 - d_o^2) = 0.43\,\text{nA}. \qquad (2)$$

Assuming that the probe size corresponds to a particular spatial frequency whose transfer was observed experimentally is of course a rather rough approximation, but it is often made in brightness determinations. In the present case, the larger image that the particle of Figure 5 came from also showed the transfer of $(123\,\text{pm})^{-1}$ spatial frequencies, but since this transfer was not strong, we did not use it for the brightness determination. A precise measurement of the gun brightness should determine the exact shape of the large-current probe experimentally, for instance by recording an image with a low probe current to characterize the object function, and then quantitatively comparing the object function to the image function recorded with a large-current probe. Investigating such a methodology is outside the scope of the present paper, but we intend to explore it in the future.

An experimentally determined value of $I_c$ leads to the normalized ("reduced") brightness $B_n$, using a conversion factor derived in [18]:

$$B_n = 8m_e e/(\pi^2 0.61^2\,h^2)I_c = 7.24 \times 10^{17}I_c, \qquad (3)$$

where $m_e$, $e$ and $h$ are the electron rest mass, electron charge, and the Planck constant, respectively, $I_c$ is specified in Amperes, and the units of $B_n$ are A/(m$^2$ sr V). In the present case, the measured normalized brightness is therefore $3.1 \times 10^8$ A/(m$^2$ sr V). This is about 3× higher than the commonly accepted CFEG normalized brightness value of $1 \times 10^8$ A/(m$^2$ sr V) (equivalent to $1 \times 10^9$ A/(cm$^2$ sr) "regular brightness" at 100 keV, e.g., [25]).

We have performed many measurements of the brightness value, spread over several months, with two different CFEG emitters, at two different microscope sites, using several different gun operating regimes, and at several different operating energies. The broad conclusions from these measurements are (1) the brightness determination described above is readily repeatable, and (2) even though the coherent current $I_c$ and the normalized brightness $B_n$ should in principle not change when the accelerating energy is changed, in practice, for a gun that is optimized for its highest accelerating energy, extracting a beam of a lower energy leads to a lower coherent current. This is partly due to the increased importance of stochastic Coulomb interactions at the lower energies, which are stronger for electrons that are accelerated less rapidly and therefore spend more time interacting with each other. It is also partly due to practical reasons that make it more difficult to parallelize the beam leaving the tip assembly as efficiently at lower accelerating energies as at high ones. This typically makes the beam entering GL1 and CL1 wider at the lower energies. The measurement of the full brightness then becomes more difficult, due to the stronger effect of the aberrations of GL1 and CL1 on a wider beam. We are still investigating this effect and ways to mitigate it. Presently it appears that the coherent current is reduced by about 1.5× at 100 keV, and even more at lower accelerating energies.

Another issue we are looking into is that when the electron beam is extracted nearly parallel from the emitter assembly, an electrode in the emitter assembly typically sits at a positive voltage of a few hundred volts relative to the emitting tip. The electrode is illuminated by the extracted beam and secondary electrons coming off the electrode can travel up the whole microscope column, and show up in EEL spectra as a small spurious peak at an energy loss corresponding to the voltage difference between the electrode and the tip. The peak is easily avoided by running the gun in a regime in which the voltage on the electrode is several thousand volts, but the beam emerging from the gun is then wider, and it is more difficult to pack currents of the order of 1 nA into very small probes. A modification of the electrode structure should make possible a gun regime optimized for high probe currents that avoids the spurious EELS peak, and we are looking into it.

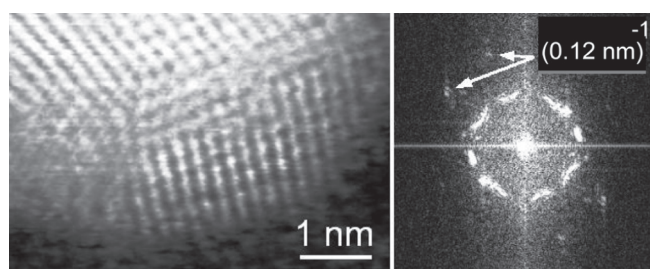A coherent current of 0.43 nA means that a probe formed with 0.43 nA and 32 mrad half-angle should be

**Fig. 6.** Part of an HAADF image of a multiply-twinned gold particle recorded at 40 keV with 60 pA beam current. The FT on the right shows captured spacings of 123 pm.

just 70 pm wide (at 200 keV), and a 1 nA probe with the same half-angle should be just 90 pm wide. We have not yet attained this level of performance, but we have come close: we were able to transfer spatial frequencies of 80 pm into an HAADF image recorded with 0.4 nA beam current, and frequencies of $(123 \text{ pm})^{-1}$ with 1.07 nA of probe current (using a smaller probe angle than optimal for the best spatial resolution). It is therefore clear that 1 nA, 100 pm (1 Å) electron probes are now not far off at 200 keV.

Figure 6 shows a part of a gold nanoparticle imaged at 40 keV with a beam current of 60 pA, and its Fourier transform. Operating at this energy lowers the knock-on threshold of carbon atoms sufficiently so that even atoms less strongly bound than in graphene sheets, e.g., those in amorphous carbon and possibly also those at the edges of graphene, cease being ejected from the lattice (in a clean vacuum). Operating at 60–80 keV is usually sufficient to avoid knock-on damage in graphene and single-layer BN, but energies even smaller than 40 keV may be useful for weakly bound structures and for very light atoms such as Be and Li.

Chromatic aberration and the longer electron wavelength worsen the smallest attainable probe size at 40 keV primary energy to about $2.5\times$ the probe size attainable at 200 keV. In order to maximize the resolution, the sample was placed about 1 mm above the lower polepiece of the 4-mm gap objective lens (OL), and the OL was run in the so-called double-crossover mode, in which there was a second crossover about 1 mm below the upper polepiece, and the beam left the objective lens nearly parallel, as it does in a condenser-objective lens. (The mode is usually called "second zone" in TEM contexts [26]. This terminology seems less suitable for STEM, in which the sample is placed in the first crossover (zone) of the lens.)

Operating in the double-crossover mode lowered the total chromatic aberration coefficient $C_c$ of the probe-forming column by about 30% relative to a single-crossover condenser-objective regime [27], and this was low enough to produce strong transfer of the $(123 \text{ pm})^{-1}$ spatial frequency. Transfer of $(123 \text{ pm})^{-1}$ spatial frequencies could be achieved in the single-crossover regime too, with the sample in the center of the objective lens, but it was significantly weaker.

The double-crossover mode is illustrated in Figure 7. For the probe-forming part of the lens, the focal length and
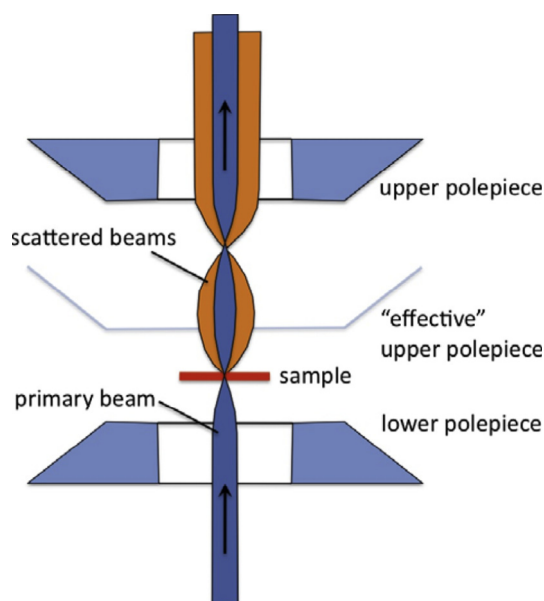


**Fig. 7.** (Color online) Schematic diagram of the electron trajectories in an objective lens operating in a double-crossover regime. The pre-sample part of the lens has properties similar to a condenser-objective lens with a lowered "effective" upper polepiece.

the aberration properties of the double-crossover regime are very similar to those of a condenser-objective lens with one half the normal gap [27]. (The best correspondence is actually obtained for slightly less than one half the normal gap, due to the fact that the magnetic field on the lens axis starts to build up already partly inside the polepieces.) The aberration properties of the post-sample part of the objective lens are worse than in the single-crossover regime, but these are much less critical in a dedicated STEM. The electron beam coming into the objective lens and going out of it has much the same properties as in the single-crossover regime, with the exception that its absolute width is narrower, because of the shorter focal length provided by the double-crossover regime. The rest of the microscope is therefore run essentially as before.

The magnetic circuit of the objective lens designed for 200 keV single-crossover operation is able to produce the increased total flux needed by the double-crossover regime at operating energies of 60 keV and lower, and could potentially be used with even more than two crossovers at lower voltages still. In this way, the aberration coefficients, especially the critical chromatic aberration coefficient, can be decreased precisely when they matter the most: at operating energies significantly lower than the microscope's maximum. At the same time, the total space available around the sample remains the same as it was with the larger OL polepiece gap designed primarily for the higher operating energies.

Figure 8 shows a single crystal of silicon imaged in the $\langle 2\,1\,1 \rangle$ direction at 200 keV, a "fat" line profile (averaged in the transverse direction) through the $(4\,4\,4)$ dumbbells visible in the HAADF image, and an FT of a larger image area. The sample was actually $\langle 1\,1\,0 \rangle$ Si, and reaching the
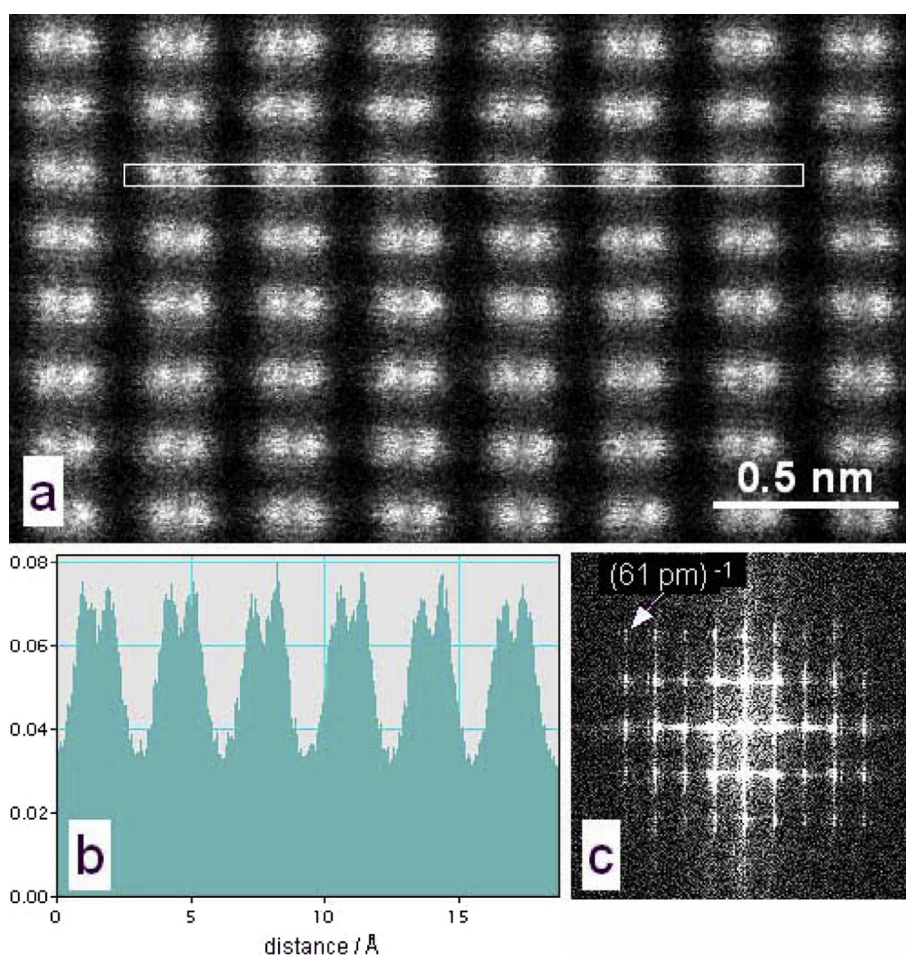
**Fig. 8.** (Color online) (a) HAADF image of single crystal Si viewed in the $\langle 2\,1\,1\rangle$ direction at 200 keV with 56 pA beam current, (b) "fat" line profile taken along the rectangle marked in (a), and (c) FT of a larger area of the image.

$\langle 2\,1\,1\rangle$ pole required a sample tilt of 30°. This was attainable in a standard double-tilt cartridge (with $\pm 25°$ tilt on each axis), by picking a $\langle 2\,1\,1\rangle$ direction that required a tilt along both $\alpha$ and $\beta$ tilt directions simultaneously. The probe current was 56 pA, a value that is useful for both imaging and energy loss spectroscopy.

The sample had essentially no amorphous material. Once a good area on the sample was found, the sample cartridge was therefore transferred from the microscope column into the storage magazine, and autotuning was performed on a combined test sample consisting of Au nanoparticles on a thin carbon film, which was available in another cartridge. Following the autotuning, the Si sample was re-introduced into the microscope column, shifted and tilted to previously saved coordinates, the position and the tilt were refined slightly, and images were recorded with no further tuning save focusing and first-order stigmating. This meant that the sample had been in the column for about 30 min when the image of Figure 8 was recorded, and a small amount of sample drift was present. The image distortion caused by the drift has been removed from the image using a dewarping algorithm, and the image has also been rotated to align the atomic rows with the edges

of the image. No image filtering was performed, which means that apart from the unwarping, the image and the line profile show as-recorded data.

The Fourier transform of the Si image shows that spatial frequencies up to $(61\text{ pm})^{-1}$ have been captured. $(4\,4\,4)$ dumbbells have been resolved in $\langle 2\,1\,1\rangle$ silicon some time ago at 300 keV using a VG HB603UX STEM equipped with a Nion aberration corrector [28] and in an FEI Titan 80-300 using a CEOS corrector [29] and more recently also in the JEOL ARM200F. The present result used a higher beam current than was typical of the other experiments, and the highest spatial frequencies were transferred more strongly.

Figure 9 shows a pair of EELS zero-loss profiles, one recorded at 100 keV primary energy, the other at 200 keV. The extraction current was 1.3 $\mu$A for the 100 keV spectrum and 0.6 $\mu$A for 200 keV spectrum, and the acquisition times were 1 s and 10 s, respectively. The full-widths at half-maximum (FWHM) of the two zero-loss (ZL) peaks are 0.26 and 0.34 eV, respectively, showing that ZL FWHM values of the order of 0.3 eV can be reached under conditions that can be used for acquiring experimental spectra. In order not to saturate the EELS
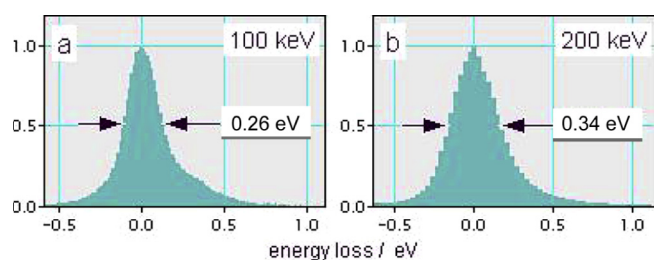
**Fig. 9.** (Color online) Zero-loss EELS profiles recorded at (a) 100 keV with 1 s integration time and (b) 200 keV with 10 s integration time.



**Fig. 10.** (Color online) Views of the electron microscope enclosure, with the principal access door closed and open.

detector, the camera length was increased so as to minimize the current entering the EELS aperture, and a high EELS energy dispersion was used.

CFEG ZL widths narrower than 0.3 eV have been recorded in the past (e.g., [30,31]), but nearly always with an emission current of the order of 0.1 $\mu$A and short acquisition times of the order of a few tens of milliseconds. Larger emission currents broaden the zero-loss width because the energy spread increases at higher cold field emission extraction voltages, and also because stronger stochastic Coulomb interactions (Boersch effect) take place near the tip and in beam crossovers with substantial beam currents. Longer acquisition times broaden the ZL peak due to instabilities in the high voltage and spectrometer power supplies. It is, however, much more informative to acquire the zero-loss profiles using acquisition parameters that are similar to those used for recording actual inner shell loss spectra, as was done here. The fact that the 200 keV ZL peak is broader than the 100 keV one points to remaining HT instabilities at 200 kV, of the order of 0.1 eV r.m.s. This amounts to an instability of 5 parts per $10^7$, and it should be possible to reduce it further in the future.

Figure 10 shows the microscope in its shielding enclosure. The left image shows the enclosure with the principal access doors closed; the right image shows it with its right access door open, as would be the case, for instance, when loading a sample magazine. A symmetrically

arranged door on the opposite side of the enclosure provides access to the microscope's virtual objective aperture (VOA), sample-level CCD TV camera, ion pump connectors, etc. For more major servicing operations such as removing and servicing whole column modules, or access to the electron gun, the front part of the enclosure (about 2/3 of the enclosure by surface area) is rolled away from the microscope, while the back part remains in place. A hermetic foam strip connects the two parts when they are in the "closed" configuration, producing an air-tight joint. The enclosure has extensive magnetic, acoustic, and thermal insulation, and serves as a bake shield when baking the microscope column. Outside surfaces of the enclosure typically stay below 60 °C during a bake, with the inside air at 120 °C and the column itself at 140 °C.

## 4 Discussion

The column of the new microscope is similar to the 100 keV column [8] that has produced a number of outstanding results (e.g., [9,11,17]). Similar performance is expected over the full range of operating energies of the new column.

Because of its enclosure, the new microscope is less sensitive to acoustic noise, short-term temperature variations, and magnetic stray fields than its 100 keV "cousin," which does not have a separate enclosure. The 100 keV version of the column is already fairly stable relative to many other microscope designs. The 200 keV column should therefore prove to be exceptionally stable, as is confirmed by the high quality of Figure 3, which was recorded with the microscope situated in a fairly noisy environment. The enclosure does not shield against *all* external disturbances – e.g., pulsation or turbulence in the cooling water, ground vibrations, low frequency acoustic noise, slow pressure changes, and long-term temperature drift will be transmitted to the microscope column very much as before. These will therefore require special attention with the new microscope.

The electron gun is new and has so far only been producing results for less than one year in its final configuration. It has attained a normalized brightness of $3.1 \times 10^8$ A/(m² sr V) at 200 keV, EELS zero-loss widths between 0.26 and 0.34 eV under operating conditions suitable for EELS spectrum acquisition, and a time interval between flash-cleanings of the tip greater than 1 h. Its level of performance is therefore limited mainly by the physics of the cold field emission process. Further improvements should be possible in the future, such as using reduced-workfunction emitters, and optimizing the aberrations of the electrostatic lens incorporated in the gun. The design appears to provide a solid foundation for these extensions.

When an electron microscope has approached 50 pm (0.5 Å) resolution, it is useful to recall a statement made by Gabor over 60 years ago [32,33]: "resolution will have to stop here (at 0.5 Å) due to lack of objects". In the STEM context this comes from the fact that at <50 pm probe size, time-averaged projected potentials of the atomic nuclei are no longer much smaller than the probe,

especially for lighter atoms, whereas HAADF imaging can only be performed at optimum efficiency with a probe that is larger than the atoms. The spatial resolution certainly still needs improving at operating energies <200 keV, but it is nevertheless worth noting that the traditionally "never-ending" quest for better and better spatial resolution in the STEM is now actually approaching the limits of the physics of the electron-matter interaction.

Very useful improvements in instrumentation will certainly be possible even when the spatial resolution limits imposed by the finite size of atoms are reached. The greatest advances can be expected in areas such as improving the EELS energy resolution with a monochromator, developing in situ experimental capabilities such as in situ heating, cooling and material deposition, adding new detectors such as secondary and Auger electron detectors, and improving the collection efficiencies of various spectroscopies such as X-rays and cathodoluminescence. We are currently pursuing several of these directions. The modular construction of the Nion column is making it much easier to implement the needed changes than if a new type of column had to be built for each new project.

A welcome feature of the described CFEG design is that because both the electrostatic and the electromagnetic gun lenses (GL0 and GL1) dissipate essentially no power (0 W for GL0, <0.1 W for GL1), the CFEG can be switched from one primary energy to another one with essentially no long-term drift resulting from the switch. The heat load in the column itself does currently change when the primary energy is switched, but even with this limitation, the Nion column is rather stable and useful data can typically be recorded at a new primary energy within less than an hour of switching. For even faster switchovers, the power supplies will have to be modified so that the microscope's lenses remain at constant power at all different primary energies rather than only for different optical regimes at each primary energy in turn, as they do now.

The microscope can run at any energy between 40 and 200 keV and can almost certainly also be set up for primary energies smaller than 40 keV. We have not explored these extra-low energy regimes yet because we have not had a suitable application for them. The only fundamental limit on the lowest possible operating energy that we are presently aware of is the efficiency of the microscope's scintillator detectors, which will start to fall off steeply below 10 keV and essentially reach zero at about 3 keV.

Another welcome feature is that by extending the operating energy of the column to 200 keV, we picked up the flexibility to run in the improved-aberrations double-crossover OL mode at energies of 60 keV and less, at no cost to the high-energy performance. Lowering the sample by 1 mm is slightly outside the range of motions for which the sample stage has been optimized, and we thus use a special sample cartridge in which the sample is lowered by about 1 mm relative to its normal position. The same capability could of course be provided for the Nion 100 keV columns, but they will then need a slightly different OL outer magnetic circuit, and a stronger OL power supply.

## 5 Conclusion

A scanning transmission electron microscope incorporating many new design elements has been built. The microscope has an exceptionally bright electron gun with a small energy spread, a very stable and flexible electron-optical column, an exceptionally stable and precise sample stage, ultra-high vacuum at the sample, a flexible configuration of efficiently coupled detectors of good sensitivity, and extensive shielding against external disturbances. Judging by its predecessor, the 100 keV Nion UltraSTEM$^{TM}$100, the new microscope is likely to open up entirely new fields of investigation. We look forward to the many exciting results it is likely to produce.

## References

1. O.L. Krivanek, N. Dellby, A.R. Lupini, Ultramicroscopy **78**, 1 (1999)
2. P.E. Batson, N. Dellby, O.L. Krivanek, Nature **418**, 617 (2002)
3. O.L. Krivanek, P.D. Nellist, N. Dellby, M.F. Murfitt, Z. Szilagyi, Ultramicroscopy **96**, 229 (2003)
4. R. Erni, M.D. Rossell, C. Kisielowski, U. Dahmen, Phys. Rev. Lett. **102**, 096101 (2009)
5. H. Sawada, Y. Tanishiro, N. Ohashi, T. Tomita, F. Hosokawa, T. Kaneyama, Y. Kondo, K. Takayanagi, J. Electron Microsc. **58**, 357 (2009)
6. P.W. Hawkes (ed.), in *Advances in Imaging and Electron Physics*, Vol. 153 (Elsevier, Amsterdam, 2008), p. 121
7. S.J. Pennycook, P.D. Nellist (eds.), *Scanning Transmission Electron Microscopy* (Springer, 2011)
8. O.L. Krivanek, G.J. Corbin, N. Dellby, B.F. Elston, R.J. Keyse, M.F. Murfitt, C.S. Own, Z.S. Szilagyi, J.W. Woodruff, Ultramicroscopy **108**, 179 (2008)
9. D.A. Muller, L.F. Kourkoutis, M.F. Murfitt, J.H. Song, H.Y. Hwang, J. Silcox, N. Dellby, O.L. Krivanek, Science **319**, 1073 (2008)
10. L.F. Kourkoutis, J.H. Song, H.Y. Hwang, D.A. Muller, Proc. Natl. Acad. Sci. **107**, 11682 (2010)
11. J. Garcia-Barriocanal, F.Y. Bruno, A. Rivera-Calzada, Z. Sefrioui, N.M. Nemes, M. Garcia-Hernández, J. Rubio-Zuazo, G.R. Castro, M. Varela, S.J. Pennycook, C. Leon, J. Santamaria, Adv. Mater. **22**, 627 (2010)

12. G.A. Botton, S. Lazar, C. Dwyer, Ultramicroscopy **110**, 926 (2010)
13. M. Terauchi, M. Tanaka, K. Tsuno, M. Ishida, J. Microsc. **194**, 203 (1999)
14. C. Mitterbauer, G. Kothleitner, W. Grogger, H. Zandbergen, B. Freitag, P. Tiemeijer, F. Hofer, Ultramicroscopy **96**, 469 (2003)
15. K. Suenaga, Y. Sato, Z. Liu, H. Kataura, T. Okazaki, K. Kimoto, H. Sawada, T. Sasaki, K. Omoto, T. Tomita, T. Kaneyama, Y. Kondo, Nat. Chem. **1**, 415 (2009)
16. O.L. Krivanek, N. Dellby, M.F. Murfitt, M.F. Chisholm, T.J. Pennycook, K. Suenaga, V. Nicolosi, Ultramicroscopy **110**, 935 (2010)
17. O.L. Krivanek, M.F. Chisholm, V. Nicolosi, T.J. Pennycook, G.J. Corbin, N. Dellby, M.F. Murfitt, C.S. Own, Z.S. Szilagyi, M.P. Oxley, S.T. Pantelides, S.J. Pennycook, Nature **464**, 571 (2010)
18. O.L. Krivanek, M.F. Chisholm, N. Dellby, M.F. Murfitt, in *Scanning Transmission Electron Microscopy*, edited by S.J. Pennycook, P.D. Nellist (Springer, 2011)
19. I.M.R. Wardell, P.E. Bovey, in *Advances in Imaging and Electron Physics*, edited by P.W. Hawkes, Vol. 159 (Elsevier, Amsterdam, 2009), p. 221
20. N. Dellby, O.L. Krivanek, M.F. Murfitt, in *Physics Procedia*, Vol. 1 (Elsevier B.V., Amsterdam, 2008), pp. 179–183
21. O.L. Krivanek, N. Dellby, M.F. Murfitt, in *Handbook of Charged Particle Optics*, edited by J. Orloff, 2nd edn. (CRC Press, 2009), pp. 601–640
22. Movie of sample motion at: http://www.nion.com/tech.html
23. O.L. Krivanek, J.P. Ursin, N.J. Bacon, G.J. Corbin, N. Dellby, P. Hrncirik, M.F. Murfitt, C.S. Own, Z.S. Szilagyi, Philos. Trans. Roy. Soc. A **367**, 3683 (2009)
24. O.L. Krivanek, N. Dellby, M.F. Murfitt, Z.S. Szilagyi, M.F. Chisholm, K. Suenaga, Proc. Microsc. Microanal. **16**, 70 (2010)
25. D.B. Williams, C.B. Carter, *Transmission Electron Microscopy*, 2nd edn. (Springer, New York, 2009), p. 74
26. H. Tochigi, H. Uchida, S. Shirai, K. Akashi, D.J. Evins, J. Bonnici, in *Proc. of 27th EMSA Meeting, 1969*, pp. 176–177
27. N. Dellby, T.C. Lovejoy, O.L. Krivanek (2011) (unpublished)
28. P.D. Nellist, M.F. Chisholm, N. Dellby, O.L. Krivanek, M.F. Murfitt, Z.S. Szilagyi, A.R. Lupini, A. Borisevich, W.H. Sides Jr., S.J. Pennycook, Science **305**, 1741 (2004)
29. H. Müller, S. Uhlemann, P. Hartel, M. Haider, Microsc. Microanal. **12**, 1 (2006)
30. O.L. Krivanek, D.N. Bui, D.A. Ray, C.B. Boothroyd, C.J. Humphreys, in *Proc. of 13th Int. EM Congress*, Vol. 1, edited by B. Jouffrey, C. Colliex (Les Éditions de Physique, Paris, 1994), p. 167
31. K. Kimoto, Y. Matsui, J. Microsc. **208**, 224 (2002)
32. D. Gabor, *The Electron Microscope* (Chemical Publishing Company, New York, 1948), p. 3
33. D.A. Muller, Nat. Mater. **8**, 263 (2009)